9.1 MASS AND WIND ANGULAR MOMENTUM RESPONSES TO MOUNTAIN TORQUES IN THE 1-25 DAY BAND. LINKS WITH THE ARCTIC OSCILLATION.

François Lott* and Fabio d'Andrea
Ecole Normale Supérieure, Laboratoire de Météorologie Dynamique, Paris, France

1. INTRODUCTION

Using the NCAR/NCEP reanalysis data, we analyze the atmospheric angular momentum *M* response to torques *T* in the 1—25 day spectral band. At these periodicities, the variations in *M* are equally distributed between variations in wind angular momentum *Mw* and mass angular momentum *Mm*. They are driven by mountain torques *Tm* which are substantially larger than the boundary layer torques *Tb*. This equi-repartition between *Mw* and *Mm* follows that the zonal flow response to *Tm* is in geostrophic balance, the major mountain ranges being located in the mid-latitudes. At these latitudes, an external positive zonal mean zonal force is in good part equilibrated by a flux of mass equatorward through the Coriolis torque, a process that increases Mm. In geostrophic balance with this mass redistribution, the zonal mean zonal wind increases where the force applies and *Mw* increases as well.

The fact that this picture explains the equi-repartition between *Mm* and Mw is confirmed by two pieces of independent evidence. The first is based on the reanalysis data, in which we evaluate the contribution of six non-overlapping latitudinal sectors to *Tm* hence varying the importance of the Coriolis torque. When the mountain torque *Tm* is produced by mountains located in the Arctic and Antarctic sectors, the changes in *Mm* dominate those in *Mw*. It is the other way round when *Tm* is produced by mountains located in the Equatorial sector and *Mm* is near *Mw* when *Tm* is due to mountains located in the subtropics or in the midlatitudes. The second is based on results from a one layer shallow water axisymmetric model on a sphere, where zonal body forces centered at different latitudes are specified. The latitudinal dependence of the repartition between *Mm* and *Mw* found in the data is reproduced by the model with *Mw* near *Mm* when the force is centered in the mid-latitudes.

The Arctic Oscillation (AO) pattern being associated with substantial *Mm* the significance of these results for the atmospheric circulation variability is also discussed. In the 1-25 day band, the AO variations are very significantly related to *Mm* variations driven by *Tm*. This result suggests that in this band the mountain ranges affect the AO variability substantially.

2. DATA DESCRIPTION

2.1 AAM budget and AO

We use 40 years (1958--1997) of the NCEP/NCAR reanalysis (Kalnay et al. 1996) to extract the daily average of the surface pressure field *Ps* the sea-level pressure field *P*, the zonal wind *u*, and the daily mean of the boundary-layer stress, τ_b. From this set of data we evaluate the global tendency budget of the atmospheric angular momentum *M*:

$$\frac{dM}{dt} = \frac{d\left(Mw + Mm\right)}{dt} = Tm + Tb \quad (1)$$

Where,

$$Mw = \int_V \rho r u \cos\theta \,.\, dV \,, \quad (2)$$

$$Mm = \int_V \rho \Omega r^2 \cos^2\theta \,.\, dV \,, \quad (3)$$

$$Tm = -\int_S Ps \frac{\partial Zs}{\partial \lambda} dS \,, \quad (4)$$

and the boundary layer torque,

$$Tb = \int_S r \cos\theta \ \tau_b \ dS \,. \quad (5)$$

In these equations V and S denotes the volume of the atmosphere and the Earth surface respectively, Ω Is the angular velocity of Earth’s rotation.

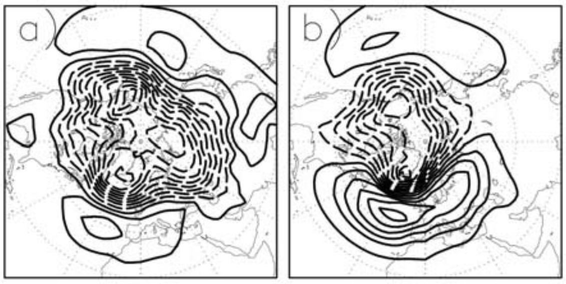

Figure 1: DJF regression of sea-level pressure maps Pm on: a) the mass angular momentum Mm (Contour Interval 0.5hPa); and b) the Arctic Oscillation index, or PC 1 of DJF Pm daily variability (Contour Interval 1hPa).

The dominant large-scale atmospheric patterns that accompany changes in mass AAM *Mm* is displayed in Fig. 1a. It shows that the Northern Hemisphere (NH) changes in global mass angular momentum are first due to a redistribution of mass from the polar latitudes to the midlatitude ones.

From this set of data, we also compute the EOFs of the sea surface pressure Pm over the Northern Hemisphere and during winter months (DJF). The first EOF (EOF 1) accounts for 9.3% of the daily DJF variability. The DJF regression of the sea level pressure *Pm* onto its PC 1 shown in Fig. 1b, is strongly reminiscent of the Arctic Oscillation (Thomson and Wallace 1998): it is strongly zonally symmetric and

---

**Corresponding author address :* LMD-ENS, 24 rue Lhomond, 75235 PARIS cedex 05, France. e-mail: flott@lmd.ens.fr associated with reinforced jets over the north east and central Pacific, as well as over the central eastern North-Atlantic. It is important to emphasize here that the two maps in Fig. 1a and Fig. 1b have a pattern correlation above 0.6, when evaluated north of 30°N. This good correlation is at the basis of the lead-lag relationships between mountain torque, mass AAM and the AO in the 20—30 day band, found in Lott et al. (2003).

2.2 Spectral analysis

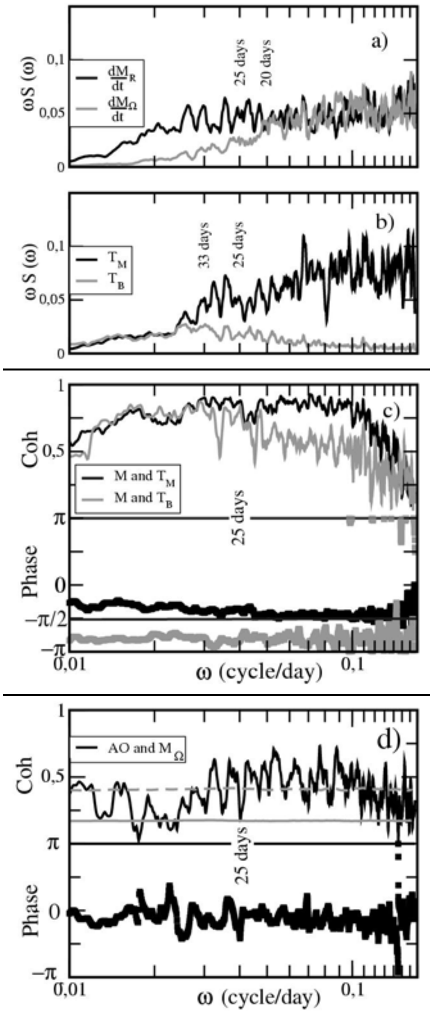

Figure 2: Spectral analysis of different terms in the AAM budget Eqs. (1)--(3). a) Spectra (S) of the *Mw* tendency (black solid) and the *Mm* tendency (grey solid). b) Spectra of *Tm* (black solid) and *Tb* (grey solid). c) Coherency (upper panel) and phase (lower panel) between the global AAM *M* and (i) *Tm* (black solid) and (ii) *Tb* (grey solid). d) Coherency (upper panel) and phase (lower panel) between the AO and *Mm*. In all curves in a), b), c), and d) a spectral smoothing window is applied to each periodigrams, yielding a resolution of $6.2\ 10^{-3}$ cy/day. In d) a median level (grey solid) and a 1% significance level (grey dashed) have also been added. They are evaluated by a Monte-Carlo procedure.

To illustrate the relevance of the high-pass 1—25 day window, Fig. 2, presents the spectra of each terms in the AAM budget Eqs. 1--3, as well as the coherence between the global AAM *M* and both torques *Tm* and *Tb.* Both spectra of *Mw* tendency (black solid in Fig. 2a) and *Mm* tendency (grey solid in Fig. 2a) present a flat background of nearly equal intensity for frequencies $\omega^{-1}<20$ day. At longer periodicities, the contribution of *Mw* exceeds that of Mm, with the latter becoming less than two times smaller than the former for $\omega^{-1}>25$ day. For the torques, the spectra in Fig. 2b show that at periodicities typically above 30-40 days, the contribution of *Tm* (black solid) and *Tb* (grey solid) is comparable, while at $\omega^{-1}<25$ day the mountain torque clearly dominates the friction torque.

The coherences and phases of the cross-spectra between the global AAM *M* and the torques *Tm* and *Tb* in Fig2c are also instructive. The rather large coherence for both torque in the upper panel of Fig.2c witnesses that the AAM budget is well closed when using the NCEP reanalysis data. The lower panel, shows that at nearly all periodicities, the mountain torque *Tm* leads *M* by almost a quarter of period, hence driving the changes in the latter (thick solid, lower panel in Fig. 2c). This lead quadrature is nearly exact at periodicities $\omega^{-1}<25$ day, that is when *Tm* dominates.

The importance of this band for the links between the mass AAM and the AO is indicated in Fig. 2d which presents a cross spectral analysis between *Mm* and the AO index. The coherence between the two series is often above *0.5* at almost all periodicities $\omega^{-1}<25$ day and again significantly below that value for $\omega^{-1}>30$day. For all periodicities the series are nearly in phase (lower panel in Fig. 2d). It is also important to emphasize that the coherence values for $\omega^{-1}<30$ day are nearly always significant at the 1%-level (grey dashed in Fig.2d) and nearly never significant for periodicities between 30 and 100 day. The coherence values are also largely above the median value of *0.17* (solid grey line) to be expected for uncorrelated series.

This discussion illustrates the specificity of the 1—25 day band to which we will concentrate in the rest of the paper. To summarize, in this band, *M* changes are little damped and predominantly driven by the mountain torque. Still in this band, the changes in *M* are almost equally distributed between *Mm* and *Mw* and the changes in *Mm* are significantly correlated with those in the AO.

3. AAM BUDGETS COMPOSITES KEYED TO 1—25 DAY SERIES

In this section, we largely use that all terms in the AAM budget Eq. 1 is linear, so it remains valid when each series of AAM and torques are filtered by a non-recursive high pass filter. Hence, we next build series of AAM and torques with substantial spectral power for periodicities, $\omega^{-1}<25$ days only, and very low power for $\omega^{-1}>35$ day. We will refer to these series as 25 day series. For the mountain torque, the standard deviation of the 25 day series is near that of the unfiltered mountain torque (not shown) while the 25 day boundary layer torque standard deviation is near 2 times smaller than that of the corresponding unfiltered series. The filter also keeps half the variance of the unfiltered mass angular momentum but strongly attenuates the standard deviation of the wind angular momentum *Mw*, which possesses a strong annual cycle. It is important to emphasize that our 25 day series, including the AO, are never small compared to the unfiltered ones.

3.1 AAM budget composites

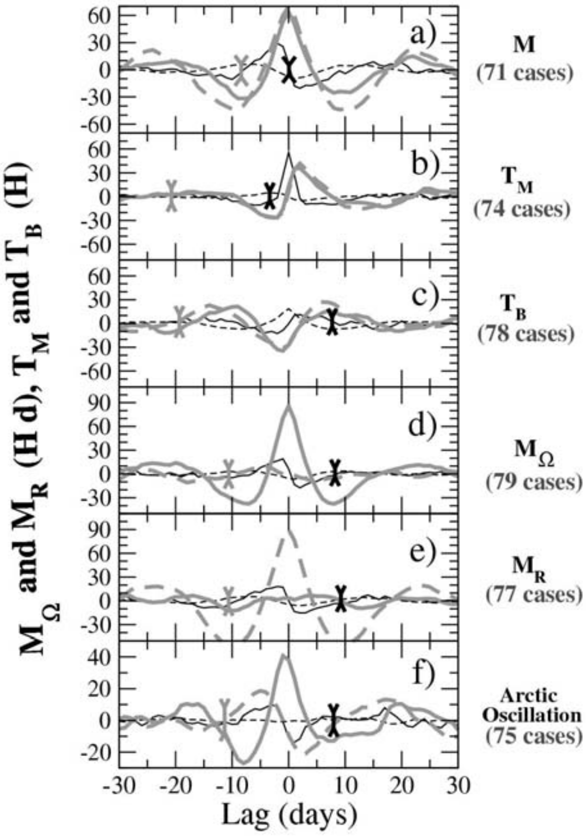

Figure 3: Composites of *Tm* (black solid), *Tb* (black dashed); *Mm* (grey solid), and *Mw* (grey dashed) keyed to 25 day series of: a) total AAM (*M*), b) mountain torque (*Tm*), c) boundary layer torque (*Tb*), d) mass AAM *Mm* e) wind AAM *Mw*, and f) *AO*. The number *N* of cases used to build the composites are given in parenthesis on the right of each panels. The black (grey) bar in each panel indicates 1% confidence level from a Monte Carlo test that uses 100 means of Tm (*Mm*), each means being made with N values of 25day *Tm* (*Mm*) taken at random.

Figures3a--f show composites of mountain torque, boundary layer torque, mass angular momentum, and wind angular momentum that are associated with distinct 25 day series, each indicated on the right of the panels. In the first panel (Fig. 3a) for instance, the composites are built from 25 days series of *Tm*, *Tb* , *Mm*, and *Mw* selected each time the 25~days AAM *M* exceeds a given positive threshold *M+* or is below a given negative threshold *M-*. The threshold values *M+=115.75Hd and M-=-124.5Hd* are used in Fig. 3a. They are about 1.5 times the standard deviation of *M* with annual cycle subtracted. In this case, *N*=71 (a value given in parenthesis). For the following composites curve Figs. 3b--f and latter in Figs. 4a--f the threshold values for the series to which the 25~day AAM budget is keyed are always chosen to ensure *60<N<80*.

The *Mm* and *Mw* composites keyed to the 25 days *M* in Fig. 3a present substantial maximum at zero lag that are of comparable amplitude. As suggested by the spectral analysis in Section2, this follows from the fact that in the 1-25 day band both *Mw* and *Mm* make comparable contributions to the global AAM *M*. The black line in Fig.3a, shows that the *M* positive anomaly at zero lag is preceded by a substantial positive mountain torque anomaly that is above *15H* for lags, *-7d<l<0d* , and followed by a subsequent negative mountain torque anomaly that is below *-15H* for lags *0d<l<7d*. Here substantial means comparable with the standard deviation of the unfiltered *Tm* series. This composite map is thus strongly suggestive that the AAM changes in the 1-25 day band are essentially driven by the mountain torque and divided between mass and wind angular momentum. To check that further, we also examined the composite of the 25~day-*Tb* keyed to the 25 day *M* (black dashed in Fig. 3a). The signal in this case is very small compared to the *Tm* composite in Fig. 3a and is in phase opposition with the *Mm* and *Mw* composites at nearly 0 day lag. This corroborates the cross-spectral results in Fig. 2c, where in the 1--25~day band the mountain torque drives the *M* changes while the friction torque damps them.

To support these points, Fig. 3b presents composites according to the 25 day *Tm*. The *Tm* (black solid) composite presents a substantial spike which lasts less than 5-6 days typically and which maximum value is almost *60H*. It is associated with rather abrupt increases in *Mm* and *Mw* centred at zero lag, that are nearly identical in phase and amplitude.

To support the hypothesis that the boundary layer torque damps the AAM anomalies, we also made composites along the 25~day *Tb* (Fig. 3b). The *Mm* and *Mw* composites are nearly in phase with each other but almost in phase opposition with the composite in *Tb*. In this case as well, the composite of the mountain torque remains the driver (black solid in Fig. 3c).

The next panel in Fig. 3d, tests what can cause changes in *Mm* only. Again the mountain torque (black solid) is the driver, and there is a surprisingly weak signal in *Mw* (grey dashed). Conversely, Fig. 3e tests what can cause changes in Mw only, giving very similar conclusion: they are driven by the mountain torque.

Finally, Fig. 3f presents composites keyed to the 25 day AO. At zero and small negative lag the AO is associated with a substantial anomaly in mass AAM (*Mm*, grey solid) whose maximum, at *l=-1d* corresponds to a strongly decreased mountain torque (black solid). It is preceded by an extremum in *Tm* close to *9H* at *l=-3d* lag and followed by a minimum in Tm close to *-14H* at *l=1d* lag (black solid). Since these extrema in *Tm* are significant (black arrow), the maximum in *Mm* is likely to be largely driven by the mountain torque.

3.2 Mountain torques evaluated over distinct latitude bands

The fact that the AAM response to mountain torques is equally distributed between mass and wind angular momentum can simply results from the fact that mountains are located in the midlatitudes, hence inducing large scale flow changes that are in geostrophic balance. If such a simple explanation is relevant to the real atmosphere, the balance between *Mw* and *Mm* must vary when the central latitude θ_0 of the mountain ranges that produce the torque varies and simply because the Coriolis parameter varies.

To check if this is the case, we next evaluate the contribution of six different non-overlapping latitudinal sectors to the mountain torque. For this, we limit the *Tm* integration in Eq. 4 to the latitude band of interest. Among the sectors selected, two cover the polar regions, the Arctic (60°N-90°N) and the Antarctic (60°S-90°S), one covers the Equatorial band (15°S-15°N) and three covers the mid and subtropical latitudes, one the Southern Hemisphere (15°S-60°S), one the subtropical northern hemisphere (15°N-35°N), and one the midlatitude northern hemisphere (35°N-60°N). The choice of these different latitude bands is somewhat arbitrary. It is motivated by the fact that the latitudinal bands need to be sufficiently large to provide substantial contributions to the mountain torque.

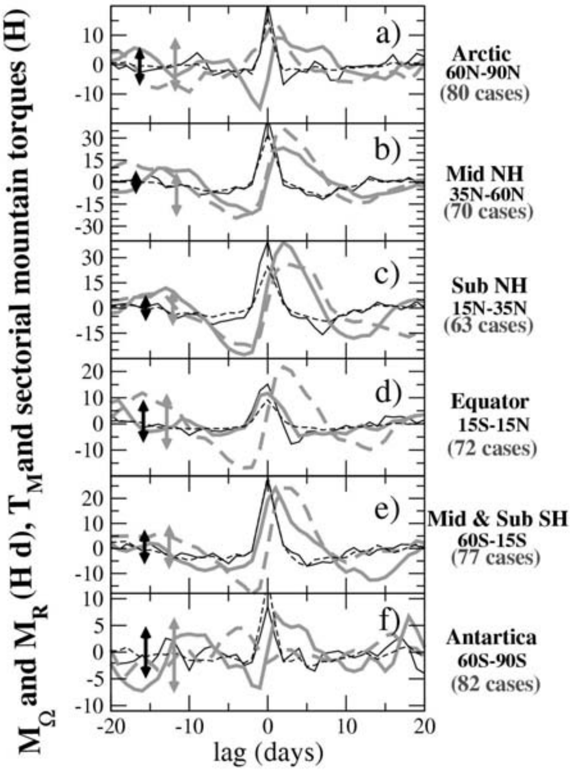

Figure 4: Composites of the 25-day AAM budget, keyed to 25~day mountain torques evaluated over 6 different non-overlapping sectors. Each sector and the number of cases taken to build the composites are given on the right of each panel. Same conventions and parameters as in Figs. 3 except that the dot black lines are for the composite of the sectorial mountain torques.

Once these series of torque have been built, they are again filtered in the 1-25 day band and composites of the AAM budget are constructed according to each of them. The composites according to the 25 day *Tm* due to the Arctic region are displayed in Fig. 4a. The global 25 day *Tm* composite (black solid) presents a significant spike that peaks at *20H* at zero lag, and that lasts around 3 days. In correspondence with this spike the mass angular momentum composites varies substantially from below *-14Hd* to *9Hd* (grey solid), while the wind angular momentum varies comparatively less (grey dashed). Away from this lag-window, none of the values of torque and AAM are significant (black and grey arrows in Fig. 4a).

A rather comparable behaviour can be seen when the contribution of Antarctica to the torque is considered Fig. 4f. It is important to note that in both Figs. 4a and 4f the extrema of mass AAM obtained at small negative and positive lag are only marginally significant. Although this can reduce the explanatory power of our interpretation, two remarks can be made. First, the change of *Mm* from a significant negative value at small negative lag to a significant positive one at small positive lag (Figs. 4a and 4f) indicates rather strong tendencies which are far more significant than the anomalies of *Mm* themselves. Second, the most pronounced changes in *Mm* in Figs. 4a and 4f occur at zero lag, and accompanied by the strongest mountain torque anomaly.

If we now return to the contribution of the Equatorial band to the mountain torque in Fig.4d, we find a behaviour that is nearly opposite to that found in the polar regions: a lag zero peak close to *15H* in *Tm* lasting nearly 6 days (black solid), corresponds within the same period to an abrupt and significant increase in the wind AAM Mw (grey dashed) while the mass AAM Mm varies moderately (grey solid) during the same interval.

When we look at the midlatitude and subtropical sectors (Figs. 4b, 4c, and 4e), significant and subsequent peaks in mountain torques lasting few days (black solid) are associated with increased *Mw* (grey dashed) and *Mm* (grey solid). Within the error bounds provided, for all these three sectors the increases in *Mm* compare in phase and amplitude with those in *Mw*.

When comparing the amplitude of the *Tm* composites in each panel of Fig. 4, it is clear that the subtropical and mid latitude make the largest contributions to the torque. This explains why the same balance holds for the global mountain torque anomalies in Fig. 3b since the subtropics and midlatitudes induce changes in *M* where *Mw* and *Mm* are comparables.

4. SHALLOW WATER MODEL FOR THE PARTITION BETWEEN Mm AND Mw

In this part, we present results in a very simple dynamical context to understand more precisely the partition between mass AAM and wind AAM. Therefore we study the zonal mean flow response to a body force acting on a zonally symmetric shallow water flow on a sphere. The set of equations used are similar to Gill (1982, p.431):

$$\left(\frac{\partial}{\partial t}+\frac{v}{r}\frac{\partial}{\partial\theta}\right)u-\left(2\Omega+\frac{u}{r\cos\theta}\right)v\sin\theta=\frac{F}{h},\quad(6)$$

$$\left(\frac{\partial}{\partial t}+\frac{v}{r}\frac{\partial}{\partial\theta}\right)v+\left(2\Omega+\frac{u}{r\cos\theta}\right)u\sin\theta=0,\quad(7)$$

$$\frac{\partial h}{\partial t}+\frac{1}{r\cos\theta}\frac{\partial hv\cos\theta}{\partial\theta}=0.\quad(8)$$

In Eq. 6, F is a body force that varies in time and latitude. Linearized around a state of rest with constant depth H_0, the Eqs. 6-8 correspond to the Laplace tidal equation for zonal wavenumber zero (Longuet-Higgins~1968).

The set of Eqs. 6-8 also satisfies an AAM budget of the form,

$$\frac{dM}{dt}=\frac{d\left(Mw+Mm\right)}{dt}=T_F\quad(9)$$

where the wind AAM, the mass AAM, and the torque due to F are:

$$M_w=2\pi r^3\int_{-\pi/2}^{+\pi/2}hu\cos^2\theta\,d\theta\quad(10)$$

$$M_m=2\pi r^4\Omega\int_{-\pi/2}^{+\pi/2}h\cos^3\theta\,d\theta\quad(11)$$

$$T_F=2\pi r^3\Omega\int_{-\pi/2}^{+\pi/2}F\cos^2\theta\,d\theta\quad(12)$$

4.1 Approximate analytical solutions

The fact that the wind AAM and the mass AAM are linked with each other via the geostrophic balance can be illustrated by two approximate solutions of the set of Eqs 6-9. In the first one the response to the torque T_F is assumed to be a uniform constant zonal wind, U, that is equilibrated by a surface elevation,

$$H=H_0+\frac{rU\Omega}{g}\left(2\cos\theta-\pi/2\right)\quad(13)$$

through the Coriolis torque. The solution in Eq. 13 is such that H and H_0 correspond to the same total mass. For this solution, and using Eqs.~10 and 11, the fraction between mass AAM and wind AAM is

$$\frac{M_m}{M_w}=\frac{r^2\Omega^2}{6gH_0}\quad(14)$$

For parameters representative of the Earth troposphere, $g=9.81\ m\ s^{-2}$, $H_0=8km$, $r=6400km$, and $\Omega=7.27\ 10^{-5}s^{-1}$ this ratio is near *0.45*.

In the second approximate solution, we assume that the mountain torque corresponds to a force applied on the flow within a very thin latitude band with width $\delta\theta << 1$ centered at a latitude θ_0. Assuming that the wind response U is constant in this band and null elsewhere, that the height response H equilibrates U in this band via the Coriolis torque, is constant elsewhere and that H and H_0 correspond to the same total mass, the fraction between mass AAM and wind AAM in this case is given by

$$\frac{M_m}{M_w}=\frac{r^2\Omega^2}{gH_0}\frac{2}{3}\sin^2\theta_0\quad(15)$$

It is null at the equator, near *1.84* at the poles and near *0.95* when θ_0 equals 45°N. This expression thus recovers at least qualitatively the latitudinal dependence between *Mm* and *Mw* found in the observations in Fig. 4.

4.2 Numerical time-dependent model

Although relevant for our study, the approximate ratios in Eqs. 14—15 rely on simplifications about the spatio temporal structure of U and H that are strongly speculative. Furthermore they do not allow to describe the transient dynamics underlying the redistribution between mass and momentum that leads to such ratios.

To evaluate these ratios in a more complete dynamical context, and for different forcings F, we next solve the set of Eqs. 6--8 with a finite difference model. Except when specified, all the experiments presented last 30 days. The forcing F is always centered on a latitude θ_0 and covers a latitude band of width $\delta\theta=10°$. In time, it starts from *0* at $t=0$ and reaches a maximum amplitude at $t=\tau_F$ and returns to zero at $t=2\tau_F$. In all experiments the value of F will be taken so that the maximum of the torque reaches $T_F(\tau_F)=10H$. In most experiments, we will also take the forcing timescale $\tau_F=2.5$ day, a value which ensures that the timescale of the response is large compared to that of the planetary gravity modes. In non-dimensional form this condition writes,

$$\left(\Omega\tau_F\right)^2=225>>\frac{r\Omega}{\sqrt{gH_0}}=1.8\quad(16)$$

For this value of τ_F we can expect that the response of the rotational modes far exceeds the gravity modes, i.e, the situation is adjusted. Nevertheless, and for completeness, we will discuss as well the response when F varies rapidly and take in one case $\tau_F=0.25$ day. In this case $\Omega\tau_F$ is near 3.

4.2 Results

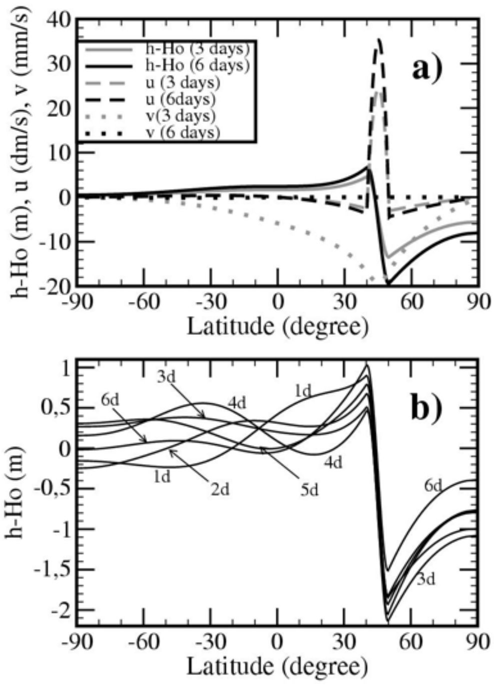

Figure 5: Shallow water model results, forcing *F* centred at θ_0=40°N. a) Slowly varying case τ_F =2.5 days: Flow profiles of h-H_0 (solid), *u* (dashed) and *v* (dot) at *t=3d* (grey) and *t=6d* (black). b) Rapidly varying case τ_F =6 hours: *h-H_0* every day.

Figure 5a shows the flow response in the slowly varying case τ_F =2.5 day, and when the forcing *F* is centered at the latitude θ_0=45°N. The response in Fig.5a is showed at two different instants, one chosen when the force *F* is non-zero (t=3 days, grey lines in Fig. 5a) and one after the force has stopped (t=6 days, black lines in Fig.~5a). At t=3 days, the positive force *F* essentially produces a meridional ageostrophic negative velocity *v* (grey dotted line) that presents a minimum near θ_0 where it does equilibrate *F* via the Coriolis torque. This southward velocity is associated with a southward flux of mass which minimum is near θ_0 as well. Accordingly, the surface elevation increases to the south of θ_0 and decreases to the north of this latitude (grey solid). In geostrophic equilibrium with *h* the zonal wind (grey dashed) presents a pronounced positive zonal jet (*u* grey dashed) in the area where *F* is non-zero and where the elevation *h* shows a strong negative gradient (between θ_0-$\delta\theta$/2=40°N and θ_0-$\delta\theta$/2=50°N). Away from that area the gradient of *h* is everywhere positive and by geostrophy *u* is negative in the northern Hemisphere and positive in the southern hemisphere.

Such a balanced description of the flow evolution stays valid as long as *F* is non-zero, and the force keeps deepening the trough in *h* north of θ_0 and raising the high south of it. Hence the zonal flow *u* keeps increasing in amplitude around θ_0. For $t>2\tau_F$, *F=0*, and the ageostrophic velocity v=0 as well (black dotted line) so the profiles of *h* (black solid) and *u* (black dashed) stay as they were at $t=2\tau_F$.

The fact that the flow no longer evolves after the forcing ends is due to that the dynamics is essentially and balanced. Indeed, for all the balanced modes, the dispersion relationship degenerate into ω=0, (see Tanaka and Kasahara 1992 for a rigorous derivation of the rotational modes in the context of tides with zonal wavenumber 0, but this is a classic behavior, see for instance the *k=0* axis of the tropical wave dispersion relationship given in Gill 1982).

In contrast, when the forcing varies rapidly τ_F =6hours (Fig. 5b) the response never reaches a steady state and some among the first gravest gravity modes are substantially excited. After the forcing end they induce planetary scale oscillations (Fig. 5b) that modulate the surface elevation around the steady response depicted in Fig. 5a.

4.d Angular momentum budget

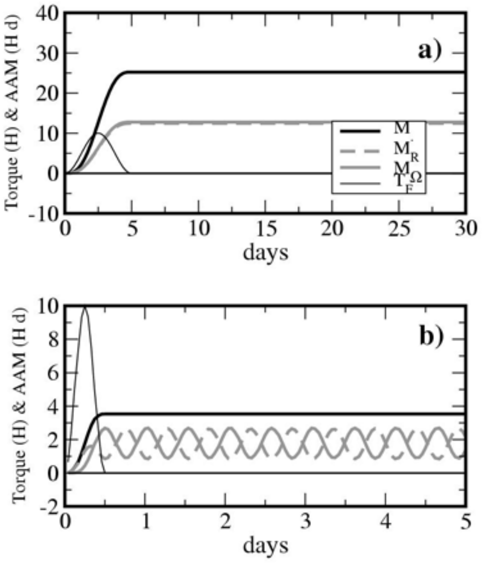

Figure 6: AAM and torque evolutions in the shallow water model, forcing F centered at 45°N: a) Slowly varying case $2\tau_F$ =5 days, b) Rapidly varying case $2\tau_F$ =12 hours. *M* (thick black), *Mm* (grey solid), *Mw* (grey dashed), and T_F (thin solid).

The evolution of the angular momentum in the slowly varying and in the rapidly varying cases described bove are presented in Fig. 6a and 6b respectively. In both cases the torque T_F (thin solid) reaches a maximum value of *10H* at t=τ_F and induces an increase in total AAM M (thick solid) that lasts $2\tau_F$. After the torque returns to 0, and *M* stays constant. In the slowly varying case in Fig. 6a, and at all time during the simulation *M* is equally distributed between *Mm* (grey solid) and *Mw* (grey dashed). In this case the change in repartition of mass seen in the profile of *h* (black solid in Fig.6a) is associated with an increase in *Mm* that equals the increase in *Mw* associated with the zonal wind *u* (black dashed in Fig. 5a) in geostrophic balance with *h*.

When the force varies rapidly, the partition between *Mw* and *Mm* never reaches a constant value (Fig. 6b). At the very beginning for instance, the force varies so fast that it induces a zonal wind acceleration instead of being equilibrated by a meridional velocity via the

Coriolis torque and *Mw* increases first (grey dashed in Fig. 6b). Rapidly, and within a time scale that compares with the inertial oscillation periodicity, *Mm* starts to increase as well to become twice larger than *Mw* at $t=2\tau_F$ =12h (grey solid). Thereafter, the presence of oscillating gravity modes in the system, makes that both *Mm* and *Mw* oscillate with a periodicity which in that case is slightly below 1 day. For both *Mw* and *Mm* these oscillations are around a mean value that is close to *M*/2 and have an amplitude that approaches as well *M/2*.

Since the dataset derived from the NCEP/NCAR reanalysis cannot sample properly oscillations with periods close to 1 day we will focus on sensitivity tests to the forcing location rather than duration. We assume that the balance dynamics at work in Fig. 5a are good enough in reality to explain our composite results in Section 3 (Figs. 3 and 4).

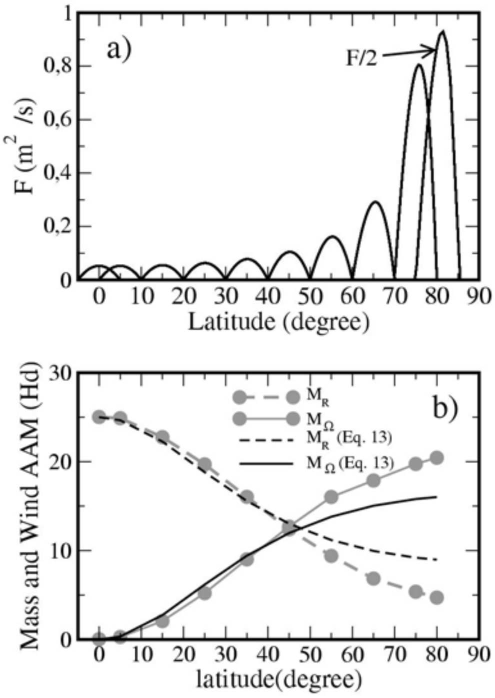

Figure 7: Sensitivity of the shallow water model response to the central latitude of the forcing *F*. a) 10 Profiles of *F* used. b) Final model values of *Mm* (grey solid with dots) and *Mw* (grey dashed with dots); theoretical values deduced from Eq. 16 are in black solid (*Mm*) and black dashed (*Mw).*

Figure 7a presents the ten profiles of *F* that have been used to test the sensitivity of our results to the latitude. The final values of *Mw* and *Mm* are displayed in Fig. 7b as a function of the forcing latitude θ_0. First, in all ten experiments, the final value of the AAM is *M=Mm+Mw=25 Hd*, which naturally follows that $T_F(\tau_F)$ is not changed from one experiment to the other. Second, the latitudinal dependence to the forcing found in the dataset in section 3 is well reproduced by the model. In particular, when the forcing is centred at the equator $\theta_0=0$ it only induces a zonal wind acceleration the Coriolis torque is very small and the AAM is almost entirely due to *Mw*.

As the forcing moves off the Equator, it induces meridional ageostrophic circulations whose importance increases as a function of latitude. As this meridional circulation directly affects the surface elevation the importance of *Mm* compared to that of *Mw* in the budget of *M* increases. When the force is centered at midlatitudes, *Mm* and *Mw* are approximatively equal. When *F* is centered at northern and polar latitudes *Mm* exceeds *Mw* substantially.

5. CONCLUSION

This study sought to identify the relative importance of wind AAM versus mass AAM into the high frequency (ω^{-1}<25 day) fluctuations in global AAM, identify the dynamical origin of this balance, and isolate one mechanism that drives high frequency fluctuations in the Arctic Oscillation. We find that the mountain torque is producing the AAM fluctuations, the friction torque being much smaller and essentially damping them. Composites anomalies of the AAM budget keyed to the 25 day mountain torque reveal that the characteristic AAM response to mountain torques is equally distributed between mass AAM and wind AAM. We interpret this result as a signature of the geostrophic balance affecting the atmospheric response to mountain torque anomalies, the major mountain ranges being located in the midlatitudes.

To corroborate this interpretation we present composite anomalies of the AAM budget keyed to mountain torques evaluated over different latitudinal sectors. When the torque is due to mountains located in the polar regions, the response in mass AAM far exceeds that in wind AAM while it is the other way round when the mountain torque is due to mountains located in the tropics. When the mountain torque is due to mountains located in the subtropics and in the midlatitudes the response in AAM is equally distributed between wind and mass AAM. As these sectors also contains the major mountain ranges, this explains why the same balance holds for the global mountain torque. This dependence to the latitude of the forcing is the first confirmation that the geostrophic balance and the Coriolis torque control the distribution of AAM between mass AAM and wind AAM.

A second evidence is provided by a one layer shallow water model for zonal flow on a rotating sphere. In this model, positive forces lasting a finite amount of time and centered at different latitudes are specified and the adjustment of the system to these forces is analyzed. When the forcings varies sufficiently slowly for that the answer to them is devoid of large scale gravity modes, the model neatly reproduces the observational results. In particular, wind and mass AAM are near equal when the force is centered around 45°N, while mass AAM exceeds wind AAM substantially when the force is moved toward the poles, and Mm is near 0 when the force is moved toward the Equator. When the forcing varies sufficiently fast so that large scale gravity modes are excited, steady values for wind and mass AAM are never obtained. Mass and wind AAM present substantial oscillations around time-mean values which fraction stays the one predicted in the slowly varying context.

The fact that the AO can be affected during the exchanges of momentum between the solid earth and the atmosphere that occur in the polar and midlatitude is quite an interesting result in itself. It follows that the AO pattern is associated with substantial mass AAM, as it corresponds to a redistribution of mass from the polar latitude to the mid latitudes (Fig. 1). This suggests that the mountain torque could be used as one of the predictors of its changes as already found by Lott et al. (2003) in the 20--30-day band. On top of the spectral coherency between the AO and mass AAM given in Fig. 2d, more quantitative evidence to support this finding are also given here. One of them is given by the composites of the AAM budget keyed to the 25 day AO in Fig. 3: they present substantial variations in mass AAM driven in good part by the mountain torque. Finally, and if we transform the surface elevation in the model results into surface pressure, the variations of 20m due to a 10H torque that lasts 5 days and that are seen in Fig.6 corresponds to surface pressure variations close to 2hPa. For torques values close to 50H consistent with the values of the composites in Figs.3-4, the surface pressure signature can easily reaches more than 10hPa: it is close to the largest pressure difference in the AO regression map in Fig. 1b.

6. ACKNOWLEDGMENT

We are gratefull of two anonymous referees of the the paper Lott and d'Andrea (2004) for suggesting the approximate solutions (Eqs. 13, 14, and 15).

7. REFERENCES

Gill, A. E., **1982**: Atmosphere-Ocean dynamics, Chapter 11, *International Geophysics Series*, Academic Press, 662p.

Kalnay, E., M. Kanamitsu, R. Kistler, W. Collins, D. Deaven, L. Gandin, M. Iredell, S. Saha, G. White, J. Woollen, Y. Zhu, A. Leetmaa, R. Reynolds, M.Chelliah, W. Ebisuzaki, W. Higgins, J. Janowiak, K.~C. Mo, C. Ropelewski, J. Wang, R. Jenne and D.~Joseph,**1996**: The NCEP/NCAR 40-year reanalysis project., *Bull. Amer. Meteor. Soc*., **77**, 437-472.

Longuet-Higgins, M. S, **1968**:The eigenfunctions of Laplace tidal equations over a sphere, *Phil. Trans. Roy. Soc. London*, **A262**, 511--607.

Lott, F., A. W. Robertson, and M.Ghil, **2003**: Mountain torques and Northern-Hemisphere low-frequency variability Part~I: Hemispheric aspects, *J. Atmos. Sci.*, In press.

Lott, F. and F. d'Andrea, **2004**: Mass and wind angular momentum responses to mountain torques in the 1-25 day band. Links with the Arctic Oscillation, *Quart. J. Roy. Meteor. Soc*., Sub-Judice.

Tanaka, H. L. and Kasahara, A. **1992**: On the normal modes of Laplace tidal equations for zonal wavenumber zero, *Tellus*, **44a**, 18—32.

Thompson, D. W., and J. M. Wallace, **1998**: The Arctic Oscillation signature in the wintertime geopotential height and temperature fields, *Geophys. Res. Lett*. bf 25, 1297-1300.